crystals

MDPI

*Article*

# Effect of $Ni^{2+}$ on Lithium-Ion Diffusion in Layered $LiNi_{1-x-y}Mn_xCo_yO_2$ Materials

**Yuanyuan Zhu [1,2,3], Yang Huang [4], Rong Du [1,2], Ming Tang [1,2], Baotian Wang [1,2,3,5] and Junrong Zhang [1,2,3,*]**

1 Institute of High Energy Physics, Chinese Academy of Sciences (CAS), Beijing 100049, China; zhuyy@ihep.ac.cn (Y.Z.); durong@ihep.ac.cn (R.D.); tangm@ihep.ac.cn (M.T.); wangbt@ihep.ac.cn (B.W.)
2 Spallation Neutron Source Science Center, Dongguan 523808, China
3 School of Nuclear Science and Technology, University of Chinese Academy of Sciences, Beijing 100049, China
4 Chongqing Institute of Green and Intelligent Technology, Chinese Academy of Sciences (CAS), Chongqing 400714, China; huangyang@ihep.ac.cn
5 Collaborative Innovation Center of Extreme Optics, Shanxi University, Taiyuan 030006, China
* Correspondence: jrzhang@ihep.ac.cn

**Abstract:** $LiNi_{1-x-y}Mn_xCo_yO_2$ materials are a typical class of layered cathode materials with excellent electrochemical performance in lithium-ion batteries. Molecular dynamics simulations are performed for $LiNi_{1-x-y}Mn_xCo_yO_2$ materials with different transition metal ratios. The Li/Ni exchange ratio, ratio of anti-site $Ni^{2+}$ to total $Ni^{2+}$, and diffusion coefficient of Li ions in these materials are calculated. The results show that the Li-ion diffusion coefficient strongly depends on the ratio of anti-site $Ni^{2+}$ to total $Ni^{2+}$ because their variation tendencies are similar. In addition, the local coordination structure of the Li/Ni anti-site is analyzed.

**Keywords:** lithium-ion batteries; Li-ion diffusion; Li/Ni anti-site; molecular dynamics

check for updates

**Citation:** Zhu, Y.; Huang, Y.; Du, R.; Tang, M.; Wang, B.; Zhang, J. Effect of $Ni^{2+}$ on Lithium-Ion Diffusion in Layered $LiNi_{1-x-y}Mn_xCo_yO_2$ Materials. *Crystals* **2021**, *11*, 465. https://doi.org/10.3390/cryst11050465

Academic Editor: Suresh Kannan Balasingam

Received: 17 March 2021
Accepted: 13 April 2021
Published: 22 April 2021

**Publisher's Note:** MDPI stays neutral with regard to jurisdictional claims in published maps and institutional affiliations.

**Copyright:** © 2021 by the authors. Licensee MDPI, Basel, Switzerland. This article is an open access article distributed under the terms and conditions of the Creative Commons Attribution (CC BY) license (https://creativecommons.org/licenses/by/4.0/).

## 1. Introduction

Lithium-ion batteries (LIBs) are promising chemical batteries, which have wide applications in mobile electronic devices and electric vehicles. It is well known that the working principle of LIBs is based on the intercalation/de-intercalation of Li ions in positive and negative electrodes during charge/discharge. Therefore, the diffusion of Li ions in the cathode and anode materials plays a dominant role in the charging and discharging ratio of LIBs [1–4]. Among the various cathode materials, layered transition metal oxides $LiNi_{1-x-y}Mn_xCo_yO_2$ (NMC) have attracted wide attention. Compared with $LiCoO_2$, $LiMn_2O_4$, and $LiNiO_2$, NMC materials have excellent electrochemical properties, such as high energy density, high reversibility, good environmental compatibility, and an excellent charge-discharge rate [5–13]. In previous studies, these electrochemical properties of NMC materials have been investigated for different transition metal (TM) ratios, including $LiNi_{1/3}Mn_{1/3}Co_{1/3}O_2$ (333) [8], $LiNi_{0.4}Mn_{0.4}Co_{0.2}O_2$ (442) [9], $LiNi_{0.5}Mn_{0.3}Co_{0.2}O_2$ (532) [10], $LiNi_{0.6}Mn_{0.2}Co_{0.2}O_2$ (622) [11], $LiNi_{0.7}Mn_{0.15}Co_{0.15}O_2$ (71515), [12] and $LiNi_{0.8}Mn_{0.1}Co_{0.1}O_2$(811) [13]. Among these electrochemical properties, the Li-ion diffusion coefficient, which is an important parameter for LIB cathode materials, directly determines the charge and discharge rate capability [14]. In particular, the rapid transportation of Li ions in cathode materials is a key factor for high-power density applications. Therefore, many experimental and theoretical studies have been conducted on the diffusion properties of Li ions in NMC materials [15–19]. For example, Yang et al. used the galvanostatic intermittent titration technique (GITT) and electrochemical impedance spectroscopy (EIS) to study the variation of the Li-ion diffusion coefficient with Li concentration in 532 [15]. In addition, Noh et al. investigated the influence of Ni content on the Li-ion diffusion coefficient of $Li[Ni_xCo_yMn_z]O_2$ (x = 1/3, 0.5, 0.6, 0.7, 0.8, 0.85) [16].

In NMC materials, Ni, Mn, and Co are distributed in the TM layer. Mn and Co primarily stabilize the interlayer structure during charging and discharging [20,21], and

Ni participates in redox behavior [22–24]. The Ni content and valence directly affect the diffusion coefficient of Li ions. Generally, Li/Ni exchange (anti-site) is formed in this system. The exchange between $Li^+$ and $Ni^{2+}$ at the 3a and 3b sites, respectively, impedes the migration path of Li ions. The anti-site $Ni^{2+}$ narrows the Li layer space, which reduces the Li-ion diffusion [25,26]. Moreover, the anti-site $Ni^{2+}$ migrates to the material surface and destroys the stability of the structure. This results in rate performance degradation and capacity fading [27,28]. However, previous studies have reported that the high $Ni^{2+}$ concentration in the TM layer is conducive to Li-ion diffusion [29,30]. As mentioned above, Li-ion diffusion can be tuned by $Ni^{2+}$ in the TM layer and the anti-site $Ni^{2+}$ in the Li layer. Thus, it is important to understand the relationship between $Ni^{2+}$ concentration and the Li-ion diffusion coefficient to optimize the layered NMC materials. Molecular dynamics (MD) can track the movement of $Li^+$, which is useful for the study of Li-ion diffusion [31–34].

In this paper, we focus on Ni-rich NMC materials because there is a significant Li/Ni exchange in them, which will impact the crystal structure and electrochemical performance of materials. We perform MD simulations of NMC materials with different TM ratios, which are $LiNi_{0.8}Mn_xCo_{0.2-x}O_2$ (x = 0, 0.05, 0.1, 0.15, 0.2), $LiNi_{0.7}Mn_xCo_{0.3-x}O_2$ (x = 0, 0.05, 0.1, 0.15, 0.2, 0.25, 0.3), $LiNi_{0.6}Mn_xCo_{0.4-x}O_2$ (x = 0, 0.05, 0.1, 0.15, 0.2, 0.25, 0.3, 0.35), and $LiNi_{0.5}Mn_xCo_{0.5-x}O_2$ (x = 0, 0.05, 0.1, 0.15, 0.2, 0.25, 0.3, 0.35, 0.4), to research the influence of $Ni^{2+}$ content on Li-ion diffusion. In Section 2, the details of the MD simulation are presented. In Section 3, the effect of $Ni^{2+}$ content on Li-ion diffusion is analyzed. In the last part, the local coordination structure of the Li/Ni anti-site is discussed.

## 2. Simulation Method

MD simulations were carried out using the DL_POLY program developed by Todorov and Smith [35]. Model building and atomic visualization were realized using CrystalMaker (CrystalMaker Software Limited, Oxfordshire, UK) [36]. In NMC materials, the Ni, Mn and Co coexist at the 3b Wyckoff position. The Ni exists as both $Ni^{2+}$ and $Ni^{3+}$, while Co and Mn stay as $Co^{3+}$ and $Mn^{4+}$, respectively. Although there is no primitive cell of NMC material in the cell database, the structure of NMC is the same as that of $LiNiO_2$. In modeling, we first obtained a 35 × 35 × 12 supercell of $LiNiO_2$ which contains 176,400 atoms in total, and then randomly substituted Ni atoms with Mn and Co atoms. The specific contents of $Ni^{2+}$, $Ni^{3+}$, $Mn^{4+}$, and $Co^{3+}$ in different NMC materials are listed in Table S1. Most NMC materials simultaneously consist of two valence states, $Ni^{2+}$ and $Ni^{3+}$, to keep the system electrically neutral [37–39]. For instance, when establishing the initial configuration of 622, 8820 $Mn^{4+}$ and 8820 $Co^{3+}$ are used to substitute the equal number of Ni atoms. As a result, the TM layer of 622 contains 8820 $Ni^{2+}$, 17640 $Ni^{3+}$, 8820 $Mn^{4+}$ and 8820 $Co^{3+}$. The stoichiometry of 622 can be written as $LiNi^{2+}_{0.2}Ni^{3+}_{0.4}Mn^{4+}_{0.2}Co^{3+}_{0.2}O_2$ [37]. The Ewald method and Verlet algorithm were used to calculate the Coulomb interactions and atomic motions, respectively [40,41]. The NVT ensemble was used in all simulations. After a lot of tests, the time required to reach equilibration was 15 ps, and the runtime of the entire simulation was 80 ps. For comparison, 442, 532, 622, and 71515 were simulated at the same temperature and state of charge (SOC) as in the work by Wei et al. [30]. For $LiNi_{0.8}Mn_xCo_{0.2-x}O_2$ (x = 0, 0.05, 0.1 0.15, 0.2), $LiNi_{0.7}Mn_xCo_{0.3-x}O_2$ (x = 0, 0.05, 0.1, 0.15, 0.2, 0.25, 0.3), $LiNi_{0.6}Mn_xCo_{0.4-x}O_2$ (x = 0, 0.05, 0.1, 0.15, 0.2, 0.25, 0.3, 0.35), and $LiNi_{0.5}Mn_xCo_{0.5-x}O_2$ (x = 0, 0.05, 0.1, 0.15, 0.2, 0.25, 0.3, 0.35, 0.4), the temperature was maintained at 1500 K, which is approximately the sintering temperature [42,43]. In addition, the temperature of 333 was maintained at 1500 K to study the local structure of the Li/Ni anti-site.

Because NMC materials are Li-doped multicomponent oxides, it is appropriate to consider the pairwise potential with partial charges for our simulations. The Morse function is often used to build bond interactions in covalent systems, which fits our potential model very well. The specific functional form is given by Equation (1) [44]

$$U(r) = Z_i Z_j e^2/r + D_{ij}[\{1 - e^{-a_{ij}(r-r_0)}\}^2 - 1] + C_{ij}/r^{12}, \quad (1)$$

where $Z_i$ and $Z_j$ are the atomic charges, $e$ is the elementary electric charge, $r$ is the interatomic distance, $D_{ij}$ represents the dissociation energy that controls the depth of the potential well, $a_{ij}$ is the parameter that controls the width of the potential well, and $C_{ij}$ is the parameter representing the finite distance at which the inter-particle potential is zero. In Equation (1), the first term refers to the Coulomb interaction, the second term to the Morse potential, and the third term to the long-range repulsive interaction. In our previous work [45], we have established a good potential field model for transition metal (TM)/lithium–oxygen interactions. It is convenient to transplant them to the Li-TM-O system of cathode materials. We used the empirical fitting method implemented in the GULP package [46] to derive the interatomic potential parameters [44]. In our strategy, the parameters are derived to reproduce the experimental crystal structures (lattice parameters and atomic positions). Table 1 lists the final potential-field parameters used in our simulations. In addition, we calculated the lattice parameters of these NMC material as shown in Figure S1, which is in good agreement with the experiment.

**Table 1.** Potential function parameters.

| Interaction | $D_{ij}$ (eV) | $r_0$ (Å) | $a_{ij}$ (Å$^{-2}$) |
|---|---|---|---|
| $Li^{+0.6} - O^{-1.2}$ | 0.001114 | 2.681360 | 3.429506 |
| $Ni^{+1.2} - O^{-1.2}$<br>$Ni^{+1.8} - O^{-1.2}$ | 0.029356 | 2.500754 | 2.679137 |
| $O^{-1.2} - O^{-1.2}$ | 0.042395 | 3.358701 | 1.659316 |
| $Mn^{+2.4} - O^{-1.2}$ | 0.029658 | 2.440000 | 3.012000 |
| $Co^{+1.8} - O^{-1.2}$ | 0.010958 | 2.400628 | 3.461272 |

In this study, the diffusion dynamics and local molecular structure of Li ions are investigated by analyzing the diffusion coefficient and defect energy of the Li/Ni anti-site. From MD simulations, we can obtain the mean square displacement (MSD) of Li-ion diffusion, as shown in Equation (2). Based on MSD, the diffusion coefficient of Li ions can be calculated using the Einstein relation as follows [47].

$$MSD(t) = \overline{|r(t) - r(t_0)|^2}, \quad (2)$$

$$D_{Li} = 1/6 \lim_{t \to \infty} d\overline{[|r(t) - r(t_0)|^2]}/dt, \quad (3)$$

where $r$ ($t$) is the position vector of a Li ion at time $t$.

To understand the local coordination structure of the Li/Ni anti-site, the defect energies were calculated with different coordination structures using the Mott−Littleton method, which was implemented in GULP. The defect energy is the difference between the total energy of the defective lattice and the perfect lattice, which is defined as:

$$E_{defect} = E_d - E_p + E_\infty, \quad (4)$$

where $E_d$ and $E_p$ are the total energies of the defective and perfect lattices, respectively. $E_\infty$ represents the energy correction of any interstitial or vacancy at infinite separation from the lattice. It is easier to form a Li/Ni anti-site with a smaller defect energy $E_{defect}$ [45]. There have been some recent studies on the calculation of the Li/TM anti-site defect [48–53], and we used the same method to calculate the Li/Ni anti-site defects in our work. In this method, a defect center is defined. Two spherical regions are divided surrounding the defect center. The ions in the inner sphere are assumed to be strongly disturbed by the defects and therefore are relaxed explicitly with respect to their Cartesian coordinates. The ions in the outer sphere are assumed to be weakly perturbed, and they can be treated implicitly as a dielectric continuum. As the radius of the inner sphere increases, these

approximations become more effective. Thus, an important stage of the defect calculation is to ensure sufficient convergence of the defect energy relative to the region radius. According to the research of Read and Jackson [54], the inner sphere radius larger than 11 Å is the most suitable, and the energy convergence reaches an optimal value when the radius of the outer sphere is twice that of the inner sphere. In our calculation, the radii of the inner and outer spheres are 13 Å and 26 Å, respectively.

## 3. Results and Discussion

### *3.1. Effect of $Ni^{2+}$ on Li-Ion Diffusion*

The space group of $LiNi_{1-x-y}Mn_xCo_yO_2$ is R-3m. Li and O atoms are located at the 3a and 6c sites, respectively. TM ion (Ni, Mn, and Co) are occupied at the 3b site. The Li, O, and TM layers are stacked layer by layer consecutively in the ABC form (O3-type), and the structure is shown in Figure 1. There are two migration pathways for Li ions in NMC materials. In one, the Li ion directly hops from one octahedral site to the next through the center of the oxygen dumbbell, called oxygen dumbbell hopping (ODH). In the other, Li ion first hops from one octahedral site to a transition state tetrahedral site and then hops to the next octahedral site, called tetrahedral site hopping (TSH) [30,55,56]. Previous studies have reported the effect owing to the type of TM ions and their valence states ($Ni^{2+}$, $Ni^{3+}$, $Co^{3+}$, and $Mn^{4+}$) [29,30]. Among these TM ions, $Ni^{2+}$ has the smallest electrostatic repulsion with migrating Li ions. According to the research by Kang et al., the activation barrier is 210 meV, which is the lowest compared with $Ni^{3+}$, $Co^{3+}$, and $Mn^{4+}$ when the nearby TM cation is $Ni^{2+}$ [30]. Therefore, regardless of the dominant diffusion path, when the migrating Li ion is close to the $Ni^{2+}$ in the TM layer, the activation barrier is very low. This suggests that a high $Ni^{2+}$ concentration in the TM layer is conducive to the diffusion of Li ions. However, $Ni^{2+}$ from the TM layer exchanges with $Li^+$ from the Li layer to form the Li/Ni anti-site defect because the ionic radii of $Ni^{2+}$ (0.69 Å) and $Li^+$ (0.76 Å) are similar. The anti-site $Ni^{2+}$ in the Li layer impedes the diffusion of Li ions. The Li/Ni exchange ratios of NMC materials with different TM ratios are calculated using the MD simulation, as shown in Figure 2 (the detailed values are listed in Table S2). It should be noted that the ratios obtained from our simulations are in good agreement with the experimental result [42,43,57–60]. It is clear that the Li/Ni exchange ratio increases with increasing $Ni^{2+}$ content (Figure 2). In addition, the Li/Ni exchange ratio also increases with increasing total Ni content when the $Ni^{2+}$ content remains the same. For example, when $x = 0.1$, the Li/Ni exchange ratios of 514, 613, 712, and 811 are 1.8%, 2.8%, 3.96%, and 5%, respectively (Table S2). According to the research of Zheng et al. [61], there are mixed valence states of $Ni^{2+}$ and $Ni^{3+}$ in Ni-rich NMC materials. A small amount of $Ni^{3+}$ transforms into the $Ni^{2+}$ state using an additional electron from the nearest $Co^{3+}$ in the TM layer. The $Co^{3+}$ changes to $Co^{4+}$ owing to the charge compensation mechanism. The higher the total Ni content, the more $Ni^{3+} \rightarrow Ni^{2+}$ transformations occur. Thus, a higher total Ni content leads to more Li/Ni anti-sites in Ni-rich materials. Essentially, it is still increasing with the amount of $Ni^{2+}$. In brief, the Li/Ni anti-sites are positively correlated with $Ni^{2+}$ content, which indicates that the structural disorder increases with increasing $Ni^{2+}$ content.

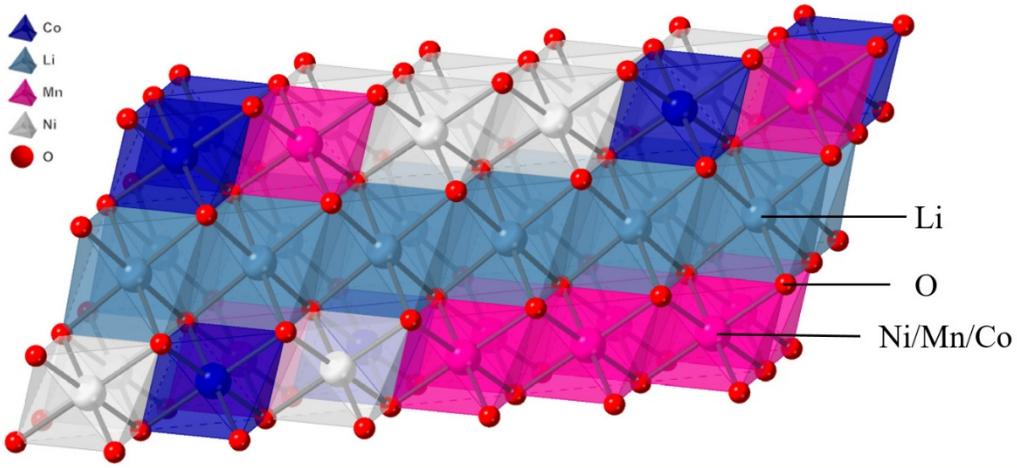



**Figure 1.** Crystal structure diagram of layered NMC materials. Ni, Mn, and Co are randomly distributed in the TM layer. Purple represents Mn, white is Ni, and dark blue is Co.

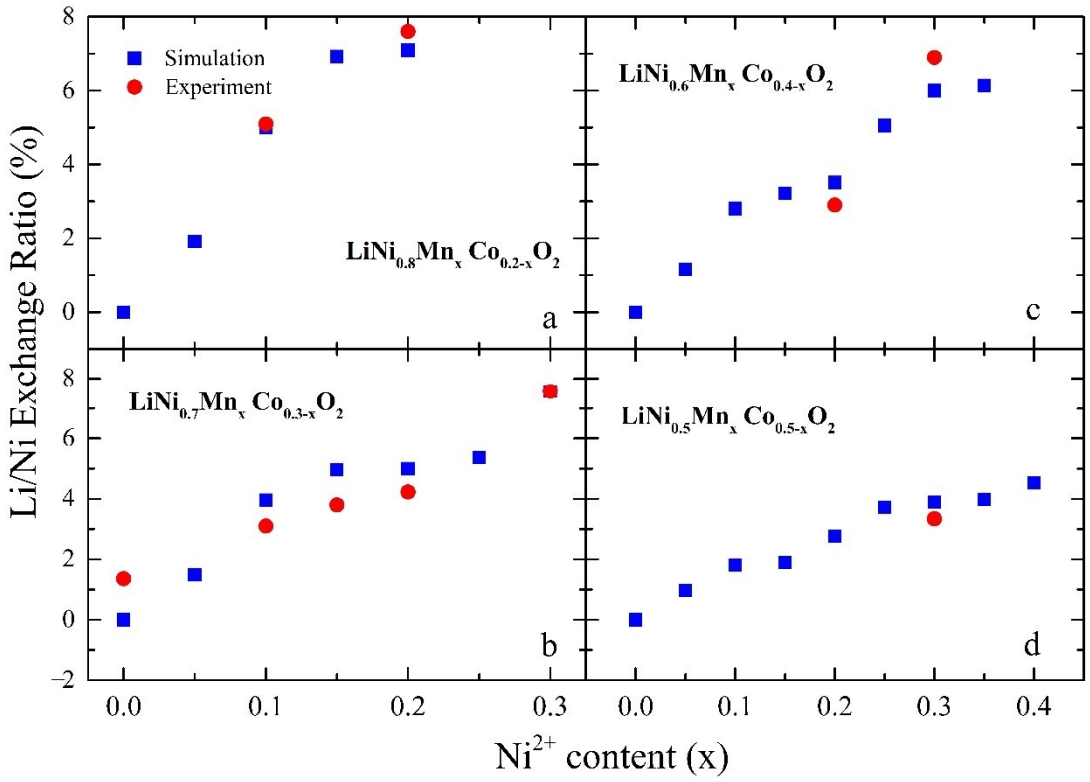



**Figure 2.** The Li/Ni exchange ratio with the content of $Ni^{2+}$ in four series of NMC materials (**a**) $LiNi_{0.8}Mn_xCo_{0.2-x}O_2$ (x = 0, 0.05, 0.1 0.15, 0.2), (**b**) $LiNi_{0.7}Mn_xCo_{0.3-x}O_2$ (x= 0, 0.05, 0.1, 0.15, 0.2, 0.25, 0.3), (**c**) $LiNi_{0.6}Mn_xCo_{0.4-x}O_2$ (x = 0, 0.05, 0.1, 0.15, 0.2, 0.25, 0.3, 0.35) and (**d**) $LiNi_{0.5}Mn_xCo_{0.5-x}O_2$ (x = 0, 0.05, 0.1, 0.15, 0.2, 0.25, 0.3, 0.35, 0.4). Blue represents the result from our simulation, and red represents experimental values from previous literature [42,43,56–59].

The same NMC materials mentioned in the study by Wei et al. [30], including 442, 532, 622, and 71515, were simulated to compare the results obtained using our method. Figure 3 shows the relationship between the Li-ion diffusion coefficient (SOC = 1/3) and the Ni content. The variation tendency of our simulation is consistent with the experiment and the ab initio molecular dynamics (AIMD) simulation, which proves the reliability of our simulation. Although there is a discrepancy of nearly two orders of magnitude between the calculated and experimental results, this difference is unavoidable due to the errors in

the experimental method and conditions [14,16,17,30]. In our work, we concentrate on the effect of $Ni^{2+}$ content on the Li-ion diffusion coefficient at SOC = 0.

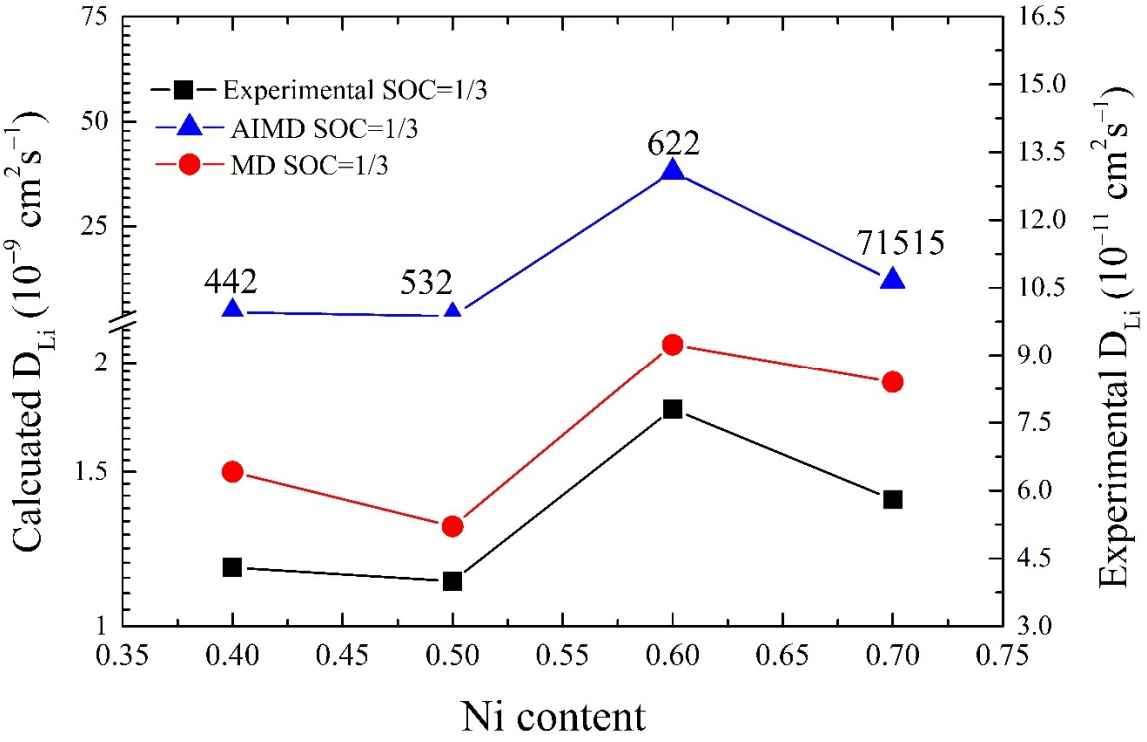



**Figure 3.** The diffusion coefficients of 442, 532, 622, and 71515. Black represents the experimental values measured by GITT [30]. Blue represents the values calculated obtained from AIMD simulations [30]. Red represents the calculated values by MD simulations in our work. It should be noted that all diffusion coefficients are obtained when SOC = 1/3.

Based on our previous discussions, there are primarily two mechanisms for tuning the diffusion of Li ions. The more $Ni^{2+}$ in the TM layer, the more conducive to the diffusion of Li ions. However, the more $Ni^{2+}$ in the TM layer would cause more Li/Ni exchange to form (Figure 2). The anti-site $Ni^{2+}$ in the Li layer hinders the transportation of Li ions. In a word, the Li-ion diffusion coefficient is tuned by the $Ni^{2+}$ of TM layer and the anti-site $Ni^{2+}$ of Li layer. The relationship between the Li-ion diffusion coefficient ($D_{Li}$) and $Ni^{2+}$ content is obtained from the MD simulation, as shown in Figure 4. For $LiNi_{0.8}Mn_xCo_{0.2-x}O_2$ (x = 0, 0.05, 0.1, 0.15, 0.2) and $LiNi_{0.7}Mn_xCo_{0.3-x}O_2$ (x = 0, 0.05, 0.1, 0.15, 0.2, 0.25, 0.3) (Figure 4a,b). The $D_{Li}$ increases from 0 $cm^2s^{-1}$ for x = 0 to $1.5 \times 10^{-8} cm^2s^{-1}$ for x = 0.15 and from 0 $cm^2s^{-1}$ for x = 0 to $1.6 \times 10^{-8}$ $cm^2s^{-1}$ for x = 0.15. It indicates that the positive effect of $Ni^{2+}$ in the TM layer on Li ion diffusion is greater than the negative effect of anti-site $Ni^{2+}$ in the Li layer when the content of $Ni^{2+}$ is low. Subsequently, $D_{Li}$ decreases from $1.5 \times 10^{-8}$ $cm^2s^{-1}$ for x = 0.15 to $1.4 \times 10^{-8}$ $cm^2s^{-1}$ for x = 0.2 and from $1.6 \times 10^{-8}$ $cm^2s^{-1}$ for x = 0.15 to $1.2 \times 10^{-8}$ $cm^2s^{-1}$ for x = 0.25. Because the $Ni^{2+}$ content continues increasing, the Li/Ni anti-site increases. The negative effect of $Ni^{2+}$ in the Li layer on Li ion diffusion increases and plays a dominant role. Moreover, there is a maximum value of $D_{Li}$ at x = 0.15 ($1.5 \times 10^{-8}$ $cm^2s^{-1}$ for $LiNi_{0.8}Mn_xCo_{0.2-x}O_2$ and $1.6 \times 10^{-8}$ $cm^2s^{-1}$ for $LiNi_{0.7}Mn_xCo_{0.3-x}O_2$). This indicates that the $Ni^{2+}$ content at x = 0.15 is the most favorable for Li-ion diffusion in these two series. In addition, the effect of $Ni^{2+}$ content on Li-ion diffusion is also slightly different, owing to the difference in the total Ni content. In Figure 4c,d, for the $LiNi_{0.6}Mn_xCo_{0.4-x}O_2$ (x = 0, 0.05, 0.1, 0.15, 0.2, 0.25, 0.3, 0.35) and $LiNi_{0.5}Mn_xCo_{0.5-x}O_2$ (x = 0, 0.05, 0.1, 0.15, 0.2, 0.25, 0.3, 0.35, 0.4), the increase range is from x = 0 to x = 0.1. The decrease areas are from x = 0.1 to x = 0.2 and from x = 0.1 to x = 0.15 in Figure 4c,d, respectively. The maximum value of $D_{Li}$ occurs at x = 0.1 ($1.5 \times 10^{-8}$ $cm^2s^{-1}$ for $LiNi_{0.6}Mn_xCo_{0.4-x}O_2$ and $1.43 \times 10^{-8} cm^2s^{-1}$ for

$LiNi_{0.5}Mn_xCo_{0.5-x}O_2$). Furthermore, when the $Ni^{2+}$ content is high ($x \geq 0.2$), $D_{Li}$ shows a tendency to first increase and then decrease.

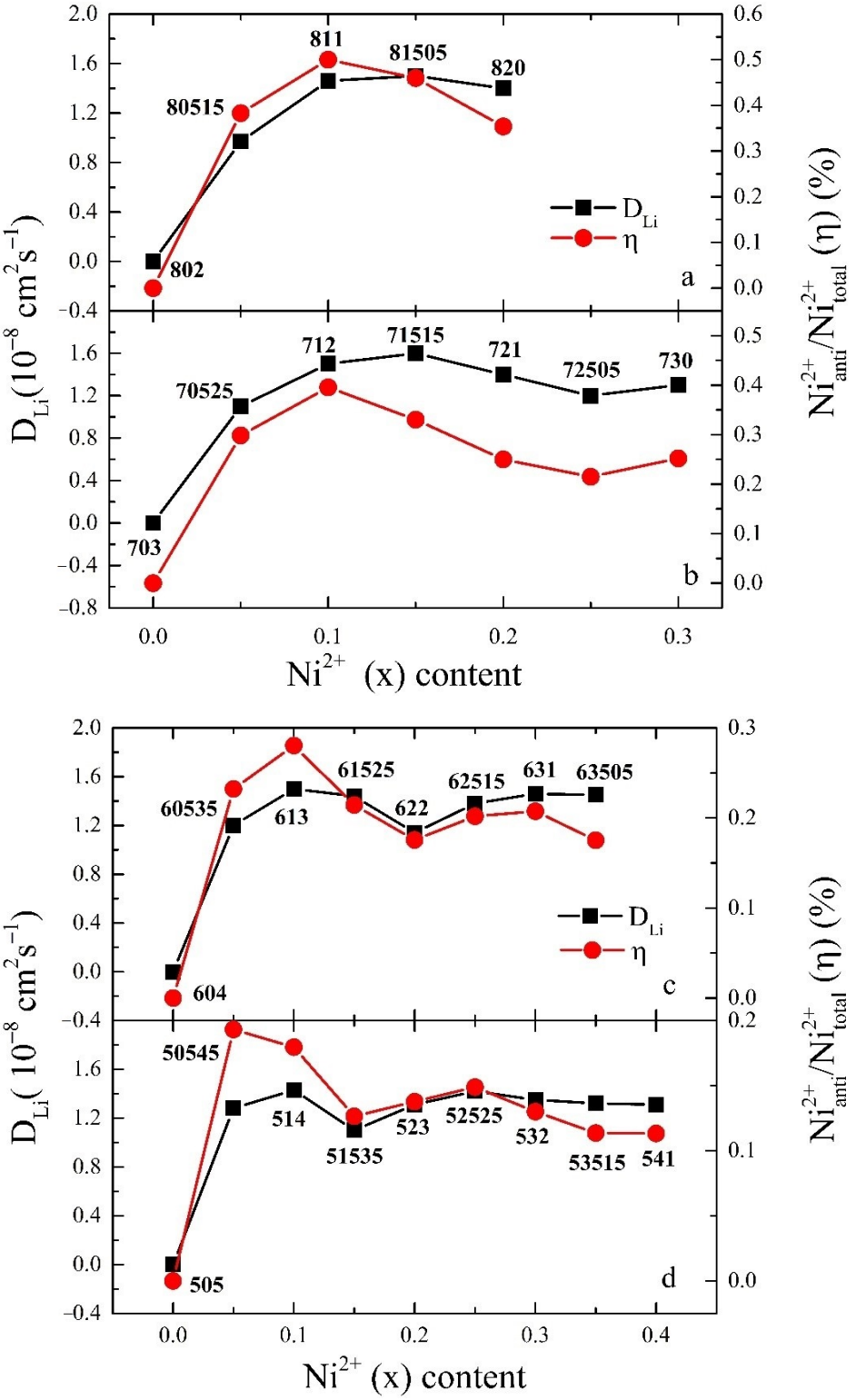



**Figure 4.** The ratio of anti-site $Ni^{2+}$ to total $Ni^{2+}$ and $D_{Li}$ in four series of NMC materials. Black represents $D_{Li}$ and red represents η. (**a**) $LiNi_{0.8}Mn_xCo_{0.2-x}O_2$ (x = 0, 0.05, 0.1 0.15, 0.2), (**b**) $LiNi_{0.7}Mn_xCo_{0.3-x}O_2$ (x = 0, 0.05, 0.1, 0.15, 0.2, 0.25, 0.3), (**c**) $LiNi_{0.6}Mn_xCo_{0.4-x}O_2$ (x = 0, 0.05, 0.1, 0.15, 0.2, 0.25, 0.3, 0.35), (**d**) $LiNi_{0.5}Mn_xCo_{0.5-x}O_2$ (x = 0, 0.05, 0.1, 0.15, 0.2, 0.25, 0.3, 0.35, 0.4).

The ratio of anti-site $Ni^{2+}$ ($Ni^{2+}_{anti}$) to total $Ni^{2+}$ ($Ni^{2+}_{total}$) is calculated for further analysis, and we named it η, which is illustrated in Figure 4. The corresponding curves exhibit the same tendency. The maximum values of the corresponding curves are not the same (Figure 4). However, they are within the range of low $Ni^{2+}$ content ($x \leq 0.15$). Within this range, there are a few Li/Ni anti-sites. $Ni^{2+}$ mainly exists in the TM layer, which facilitates the diffusion of Li ions. Taking the case of $LiNi_{0.7}Mn_xCo_{0.3-x}O_2$ ($x = 0$, 0.05, 0.1, 0.15, 0.2, 0.25, 0.3) as an example, in Figure 4b, $D_{Li}$ reaches its maximum value at $x = 0.15$, while η is maximized at $x = 0.1$. The $D_{Li}$ of 71515 is greater than that of 712, which can be explained by their corresponding η. Although both the $Ni^{2+}_{anti}$ and $Ni^{2+}_{total}$ of 71515 are higher than that of 712, the value of η of 71515 is smaller than that of 712 (Figure 4b). Thus, there is more $Ni^{2+}$ left in the TM layer of 71515 than of 712. $Ni^{2+}$ in the TM layer is beneficial for the diffusion of Li ions. Thus, the $D_{Li}$ of 71515 is greater than that of 712 (Figure 4b), which is consistent with the previous discussion. The facilitating effect caused by $Ni^{2+}$ in the TM layer plays a leading role when the $Ni^{2+}$ content is low ($x \leq 0.15$). Thus, the $D_{Li}$ of 71515 is greater than that of 721 (Figure 4b). As the $Ni^{2+}$ content continues increasing, η begins to decline and reaches a minimum value. The minimum values of $D_{Li}$ and η correspond to each other in Figure 4. This indicates that Li-ion diffusion is more impeded by a smaller η. As discussed above, the impeding effect caused by the anti-site $Ni^{2+}$ in the Li layer plays a dominant role when the $Ni^{2+}$ content is high ($x \geq 0.2$). In a word, $D_{Li}$ depends strongly on η, especially when the $Ni^{2+}$ concentration is high ($x \geq 0.2$). $D_{Li}$ is positively correlated to η.

### *3.2. Local Coordination Structure of Li/Ni Anti-Site*

The formation of the Li/Ni anti-site indicates a change in the local coordination structure, as shown in Figure 5. Before the Li/Ni anti-site, the Ni ion is surrounded by the six nearest TM ions in the TM layer and is located in the center of a hexagon composed of these six TM ions. After the Li/Ni anti-site, the anti-site Li ion is located in the center of these six TM ions. The anti-site Ni ion connects to the five nearest TM ions and one Li ion in the upside TM layer, and six nearest TM ions in the downside TM layer via intermediate oxygen atoms. In this work, 333 is chosen for further investigation as it contains the same contents of Ni, Mn, and Co. We calculated the defect energy of different local coordination environments, in which the number of Mn ions increased from zero to six. Moreover, we also considered the influence of different arrangements on the defect energy when the numbers of Ni, Mn, and Co are determined. Thus, the defect energies of all the cases were calculated. The result is illustrated in Figure 6, which is supported by the research of Lee et al. The defect energy of the Li/Ni anti-site is approximately 0.84 eV, which is consistent with our calculation [62]. As shown in Figure 6, the defect energy ($E_d$ ) exhibits a downward tendency with an increasing number of Mn ions. When there are few Mn ions (Figure 6a–c), $E_d$ is typically high. This is not conducive to the stable existence of the Li/Ni anti-site. When the number of Mn ions is in the majority (Figure 6e–g), $E_d$ is generally low. This is favorable for the formation of the Li/Ni anti-site. Additionally, we calculated the variation in the defect energy with the increasing number of Co ions. The results are presented in Figure 7. $E_d$ exhibits no evident increase or decrease tendency with an increasing Co number from Figure 7a–g. However, $E_d$ changes significantly at the same Co number. For instance, in Figure 7b, which contains one Co ion, $E_d$ exhibits a tendency to decline when the Mn number increases from left to right. This means that it is easy to form the Li/Ni anti-site when Mn ions are in the majority among the six TM ions which surround the Ni ion. Furthermore, in both Figures 6 and 7, the defect energy of the Li/Ni anti-site is different when the Ni, Mn, and Co numbers are confirmed. This reveals that different arrangements influence the $E_d$ of the Li/Ni anti-site.

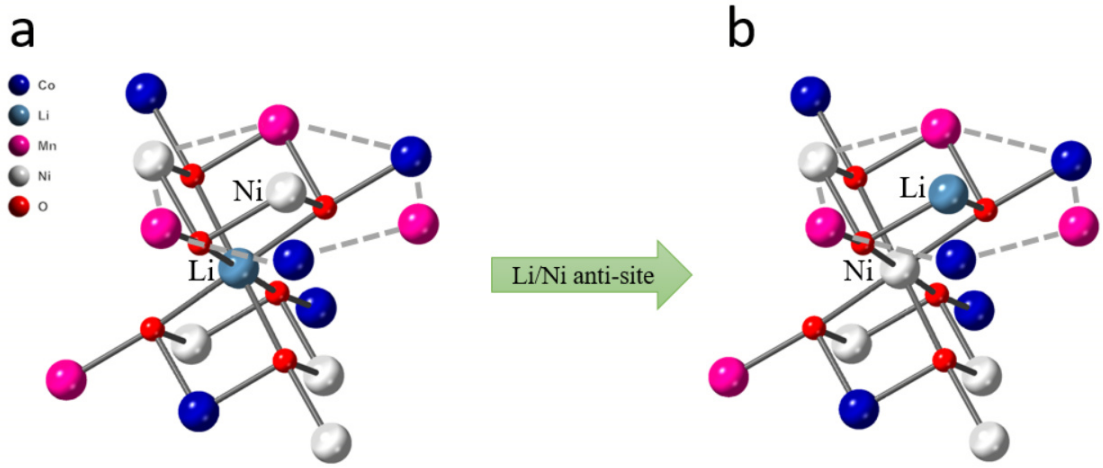



**Figure 5.** The local coordination structure of Li/Ni anti-site. (**a**) Before Li/Ni anti-site, (**b**) after Li/Ni anti-site. Purple represents Mn, white represents Ni, dark blue represents Co, light blue represents Li, and red represents O.

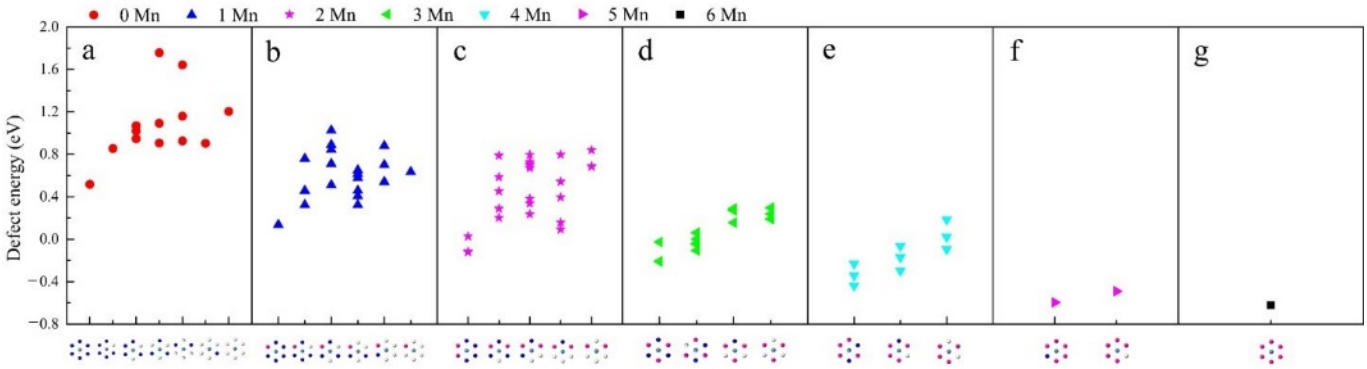



**Figure 6.** The defect energy of the Li/Ni anti-site with different local coordination environments. From (**a**–**g**), the Mn number of six local TM ions increases in turn. The schematics at the bottom represent the local coordination ion environment for the anti-site Li-ion in the TM layer. For one schematic of the bottom, the different points of the longitudinal axis represent the defect energy of various arrangements under the corresponding number of Ni, Mn, and Co.

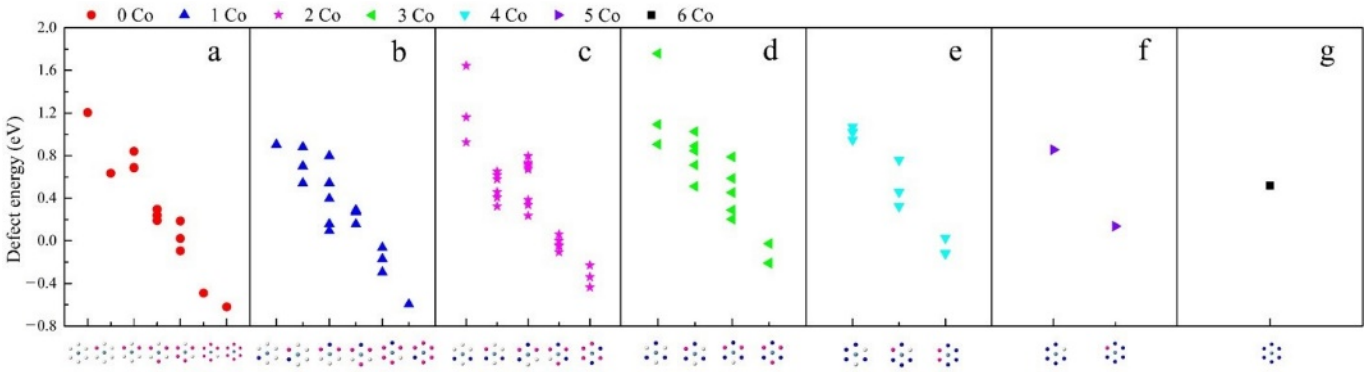



**Figure 7.** The defect energy of Li/Ni anti-site with different local coordination environments. From (**a**–**g**), the Co number of six local TM ions increases in turn. The Mn number increases from left to right under the same Co number.

## 4. Conclusions

In this article, we performed MD simulations to investigate the influence of $Ni^{2+}$ on Li-ion diffusion in layered $LiNi_{1-x-y}Mn_xCo_yO_2$ with Li/Ni anti-sites. Firstly, the Li-ion diffusion coefficients of NMC materials with different TM ratios were calculated. We found a peak value for the Li-ion diffusion coefficient with increasing $Ni^{2+}$ content in each series

of NMC materials. Then, we calculated the ratio of the anti-site $Ni^{2+}$ to total $Ni^{2+}$. The variation tendency of this ratio is consistent with that of the Li-ion diffusion coefficient. This indicates that the Li-ion diffusion coefficient strongly depends on the ratio of anti-site $Ni^{2+}$ to total $Ni^{2+}$. Besides, by calculating the defect energy of the Li/Ni anti-site for different local coordination environments, we found that it is easy to form the Li/Ni anti-site when Mn ions are in the majority among the six TM ions which surround the Ni ion. According to our research, an appropriate $Ni^{2+}$ can be selected to maximize the diffusion of Li ions, which is of great significance for the design and optimization of layered NMC materials.

**Supplementary Materials:** The following are available online at https://www.mdpi.com/article/10.3390/cryst11050465/s1, Table S1: $LiNi_{1-x-y}Mn_xCo_yO_2$ materials with different TM ratios in this work. $LiNi_{0.8}Mn_xCo_{0.2-x}O_2$(x = 0, 0.05, 0.1 0.15, 0.2), $LiNi_{0.7}Mn_xCo_{0.3-x}O_2$ (x = 0, 0.05, 0.1, 0.15, 0.2, 0.25, 0.3), $LiNi_{0.6}Mn_xCo_{0.4-x}O_2$ (x = 0, 0.05, 0.1, 0.15, 0.2, 0.25, 0.3, 0.35), and $LiNi_{0.5}Mn_xCo_{0.5-x}O_2$ (x = 0, 0.05, 0.1, 0.15, 0.2, 0.25, 0.3, 0.35, 0.4). Table S2: The value of the Li/Ni exchange ratio, for $LiNi_{0.8}Mn_xCo_{0.2-x}O_2$(x = 0, 0.05, 0.1 0.15, 0.2), $LiNi_{0.7}Mn_xCo_{0.3-x}O_2$ (x = 0, 0.05, 0.1, 0.15, 0.2, 0.25, 0.3), $LiNi_{0.6}Mn_xCo_{0.4-x}O_2$ (x = 0, 0.05, 0.1, 0.15, 0.2, 0.25, 0.3, 0.35), and $LiNi_{0.5}Mn_xCo_{0.5-x}O_2$ (x = 0, 0.05, 0.1, 0.15, 0.2, 0.25, 0.3, 0.35, 0.4). Figure S1: The comparison of lattice parameters between MD simulations and experimental values.

**Author Contributions:** Formal analysis and writing—original draft, Y.Z.; methodology, Y.H.; software, R.D. and M.T.; writing—review and editing, J.Z.; resources, B.W.; funding acquisition and supervision, J.Z.; All authors have read and agreed to the published version of the manuscript.

**Funding:** This research was supported by the National Natural Science Foundation of China (Grant No.11675195), the National Key R&D Program of China (2017YFA0403700), and Key Research Program of Frontier Sciences, CAS, Grant No. 292016YQYKXJ00135.

**Institutional Review Board Statement:** Not applicable.

**Informed Consent Statement:** Informed consent was obtained from all subjects involved in the study.

**Conflicts of Interest:** The authors declare no conflict of interest.

## References

1. Xu, B.; Qian, D.; Wang, Z.; Meng, Y.S. Recent progress in cathode materials research for advanced lithium ion batteries. *Mater. Sci. Eng. R* **2012**, *73*, 51–65. [CrossRef]
2. Lu, L.; Han, X.; Li, J.; Hua, J.; Ouyang, M. A review on the key issues for lithium-ion battery management in electric vehicles. *J. Power Source* **2013**, *226*, 272–288. [CrossRef]
3. Zhao, E.; He, L.; Wang, B.; Li, X.; Zhang, J.; Wu, Y.; Chen, J.; Zhang, S.; Liang, T.; Chen, Y.; et al. Structural and mechanistic revelations on high capacity cation-disordered Li-rich oxides for rechargeable Li-ion batteries. *Energy Storage Mater.* **2019**, *16*, 354–363. [CrossRef]
4. Huang, Y.-R.; Chen, C.-L.; Pu, N.-W.; Wu, C.-H.; Liu, Y.-M.; Chen, Y.-H.; Youh, M.-J.; Ger, M.-D. Experimental and Modeling Analysis of Holey Graphene Electrodes for High-Power-Density Li-Ion Batteries. *Crystals* **2020**, *10*, 1063. [CrossRef]
5. Manthiram, A.; Song, B.; Li, W. A perspective on nickel-rich layered oxide cathodes for lithium-ion batteries. *Energy Storage Mater.* **2017**, *6*, 125–139. [CrossRef]
6. Schipper, F.; Erickson, E.M.; Erk, C.; Shin, J.-Y.; Chesneau, F.F.; Aurbach, D. Review—Recent Advances and Remaining Challenges for Lithium Ion Battery Cathodes I. Nickel-Rich, $LiNi_xCo_yMn_zO_2$. *J. Electrochem. Soc.* **2017**, *164*, A6220–A6228. [CrossRef]
7. Tuccillo, M.; Palumbo, O.; Pavone, M.; Muñoz-García, A.B.; Paolone, A.; Brutti, S. Analysis of the Phase Stability of $LiMO_2$ Layered Oxides (M = Co, Mn, Ni). *Crystals* **2020**, *10*, 526. [CrossRef]
8. Wang, J.-H.; Wang, Y.; Guo, Y.-Z.; Liu, C.-W.; Dan, L.-L. Electrochemical characterization of $AlPO_4$ coated $LiNi_{1/3}Co_{1/3}Mn_{1/3}O_2$ cathode materials for high temperature lithium battery application. *Rare Met.* **2014**, *40*, 78–83. [CrossRef]
9. Satyanarayana, M.; James, J.; Varadaraju, U.V. Electrochemical performance of $LiNi_{0.4}Co_{0.2}Mn_{0.4}O_2$ prepared by different molten salt flux: $LiNO_3$-LiCl and $LiNO_3$-$KNO_3$. *Appl. Surf. Sci.* **2017**, *418*, 72–78.
10. Zhao, X.; Liu, B.; Yang, J.; Hou, J.; Wang, Y.; Zhu, Y.; Zhao, X.; Liu, B.; Yang, J.; Hou, J.; et al. Synthesizing $LiNi_{0.5}$ $Co_{0.2}Mn_{0.3}O_2$ with microsized peanut-like structure for enhanced electrochemical properties of lithium ion batteries. *J. Alloys Compd.* **2020**, *832*, 154464. [CrossRef]
11. Chen, Y.; Tang, S.; Deng, S.; Lei, T.; Li, Y.; Li, W.; Cao, G.; Zhu, J.; Zhang, J. Chemical coupling constructs amorphous silica modified $LiNi_{0.6}Co_{0.2}Mn_{0.2}O_2$ cathode materials and its electrochemical performances. *J. Power Source* **2019**, *431*, 8–16. [CrossRef]

12. Li, W.; Li, Y.; Yang, L.; Chen, Y.; Guo, J.; Zhu, J.; Cao, G.L. Enhancing high-voltage electrochemical performance of $LiNi_{0.7}Mn_{0.15}Co_{0.15}O_2$ cathode materials with SiO2 coatings via electrostatic attraction forces method. *Ionics* **2020**, *26*, 5393–5403. [CrossRef]
13. Liang, J.; Lu, Y.; Wang, J.; Liu, X.; Chen, K.; Ji, W.; Zhu, Y.; Wang, D. Well-ordered layered $LiNi_{0.8}Co_{0.1}Mn_{0.1}O_2$ submicron sphere with fast electrochemical kinetics for cathodic lithium storage. *J. Energy Chem.* **2020**, *47*, 188–195. [CrossRef]
14. Park, M.; Zhang, X.; Chung, M.; Less, G.B.; Sastry, A.M. A review of conduction phenomena in Li-ion batteries. *J. Power Source* **2010**, *195*, 7904–7929. [CrossRef]
15. Yang, S.; Wang, X.; Yang, X.; Bai, Y.; Liu, Z.; Shu, H.; Wei, Q. Determination of the chemical diffusion coefficient of lithium ions in spherical $Li[Ni_{0.5}Mn_{0.3}Co_{0.2}]O_2$. *Electrochim. Acta* **2012**, *66*, 88–93. [CrossRef]
16. Noh, H.J.; Youn, S.; Yoon, C.S.; Sun, Y.K. Comparison of the structural and electrochemical properties of layered $Li[Ni_xCo_yMn_z]O_2$ (x = 1/3, 0.5, 0.6, 0.7, 0.8 and 0.85) cathode material for lithium-ion batteries. *J. Power Source* **2013**, *233*, 121–130. [CrossRef]
17. Li, Z.; Ban, C.; Chernova, N.A.; Wu, Z.; Upreti, S.; Dillon, A.; Whittingham, M.S. Towards understanding the rate capability of layered transition metal oxides. *J. Power Source* **2014**, *268*, 106–112. [CrossRef]
18. Gao, A.; Sun, Y.; Zhang, Q.; Zheng, J.; Lu, X. Evolution of Ni/Li antisites under the phase transition of a layered $LiNi_{1/3}Co_{1/3}Mn_{1/3}O_2$ cathode. *J. Mater. Chem. A* **2020**, *8*, 6337–6348. [CrossRef]
19. Cui, S.; Wei, Y.; Liu, T.; Deng, W.; Hu, Z.; Su, Y.; Li, H.; Li, M.; Guo, H.; Duan, Y.; et al. Optimized Temperature Effect of Li-Ion Diffusion with Layer Distance in $Li(Ni_xMn_yCo_z)O_2$ Cathode Materials for High Performance Li-Ion Battery. *Adv. Energy Mater.* **2016**, *6*, 1501309. [CrossRef]
20. Yamada, A.; Tanaka, M.; Tanaka, K.; Sekai, K. Jahn–Teller instability in spinel Li–Mn–O. *J. Power Source* **1999**, *81–82*, 73–78. [CrossRef]
21. Ellis, B.L.; Lee, K.T.; Nazar, L.F. Positive Electrode Materials for Li-Ion and Li-Batteries. *Chem. Mater.* **2010**, *22*, 691–714. [CrossRef]
22. Guo, J.; Jiao, L.F.; Yuan, H.T.; Li, H.X.; Zhang, M.; Wang, Y.M. Effect of synthesis condition on the structural and electrochemical properties of $Li[Ni_{1/3}Mn_{1/3}Co_{1/3}]O_2$ prepared by the metal acetates decomposition method. *Electrochim. Acta* **2006**, *51*, 3731–3735. [CrossRef]
23. Hwang, B.J.; Santhanam, R.; Chen, C.H. Effect of synthesis conditions on electrochemical properties of $LiNi_{1-y}Co_yO_2$ cathode for lithium rechargeable batteries. *J. Power Source* **2003**, *114*, 244–252. [CrossRef]
24. Ren, H.; Huang, Y.; Wang, Y.; Li, Z.; Cai, P.; Peng, Z.; Zhou, Y. Effects of different carbonate precipitators on $LiNi_{1/3}Co_{1/3}Mn_{1/3}O_2$ morphology and electrochemical performance. *Mater. Chem. Phys.* **2009**, *117*, 41–45. [CrossRef]
25. Kang, K.; Ceder, G. Factors that affect Li mobility in layered lithium transition metal oxides. *Phys. Rev. B* **2006**, *74*, 094105. [CrossRef]
26. Yu, H.; Qian, Y.; Otani, M.; Tang, D.; Guo, S.; Zhu, Y.; Zhou, H. Study of the lithium/nickel ions exchange in the layered $LiNi_{0.42}Mn_{0.42}Co_{0.16}O_2$ cathode material for lithium ion batteries: Experimental and firstprinciples calculations. *Energy Environ. Sci.* **2014**, *7*, 1068–1078. [CrossRef]
27. Yan, P.; Nie, A.; Zheng, J.; Zhou, Y.; Lu, D.; Zhang, X.; Xu, R.; Belharouak, I.; Zu, X.; Xiao, J.; et al. Evolution of Lattice Structure and Chemical Composition of the Surface Reconstruction Layer in $Li_{1.2}Ni_{0.2}Mn_{0.6}O_2$ Cathode Material for Lithium Ion Batteries. *Nano Lett.* **2015**, *15*, 514–522. [CrossRef]
28. Yan, P.; Zheng, J.; Lv, D.; Wei, Y.; Zheng, J.; Wang, Z.; Kuppan, S.; Yu, J.; Luo, L.; Edwards, D.; et al. Atomic-Resolution Visualization of Distinctive Chemical Mixing Behavior of Ni, Co, and Mn with Li in Layered Lithium Transition-Metal Oxide Cathode Materials. *Chem. Mater.* **2015**, *27*, 5393–5401. [CrossRef]
29. Kang, K.; Meng, Y.S.; Breger, J.; Grey, C.P.; Ceder, G. Electrodes with High Power and High Capacity for Rechargeable Lithium Batteries. *Science* **2006**, *311*, 977–980. [CrossRef]
30. Wei, Y.; Zheng, J.; Cui, S.; Song, X.; Su, Y.; Deng, W.; Wu, Z.; Wang, X.; Wang, W.; Rao, M.; et al. Kinetics Tuning of Li-Ion Diffusion in Layered $Li(Ni_xMn_yCo_z)O_2$. *J. Am. Chem. Soc.* **2015**, *137*, 8364–8367. [CrossRef]
31. Lychagin, D.; Dmitriev, A.; Nikonov, A. Alfyorova, Crystallographic and Geometric Factors in the Shear Development in <001> FCC Single Crystals: Molecular Dynamics Simulation and Experimental Study. *Crystals* **2020**, *10*, 666. [CrossRef]
32. Wang, B.-B.; Xiao, Y.; Xu, Z.-M. Variation in Properties of Pre-Nucleation Calcium Carbonate Clusters Induced by Aggregation: A Molecular Dynamics Study. *Crystals* **2021**, *11*, 102. [CrossRef]
33. Hu, B.; Tao, G. Molecular Dynamics Simulations on Lithium Diffusion in $LiFePO_4$: The effect of anti-site defects. *J. Mater. Chem. A* **2015**, *3*, 20399–20407. [CrossRef]
34. Tateishi, K.; du Boulay, D.; Ishizawa, N. The effect of mixed Mn valences on Li migration in $LiMn_2O_4$ spinel: A molecular dynamics study. *Appl. Phys. Lett.* **2004**, *84*, 529–531. [CrossRef]
35. Smith, W.; Forester, T.R.; Todorov, I.T. *The DL_POLY_4 User Manual*; Version 4.08; STFC Daresbury Laboratory Daresbury: Warrington, UK, 2016.
36. CrystalMaker Software Ltd., Centre for Innovation & Enterprise, Begbroke Science Park, Woodstock Road, Begbroke, Oxfordshire, OX5 1PF, UK. Available online: http://www.crystalmaker.com (accessed on 15 April 2021).
37. Ahn, W.; Lim, S.N.; Jung, K.-N.; Yeon, S.-H.; Kim, K.-B.; Song, H.S.; Shin, K.-H. Combustion-synthesized $LiNi_{0.6}Mn_{0.2}Co_{0.2}O_2$ as cathode material for lithium ion batteries. *J. Alloys Compd.* **2014**, *609*, 143–149. [CrossRef]
38. Guo, J.; Hu, C.Y. Synthesis of nanosized $LiNi_{0.7}Mn_{0.2}Co_{0.1}O_2$ cathode material for lithium ion batteries by combination method of forced hydrolytic and hydroxide coprecipitation. *Mater. Res. Innov.* **2014**, *19*, 238–243. [CrossRef]

39. Kosova, N.V.; Devyatkina, E.T.; Kaichev, V.V. Optimization of $Ni^{2+}/Ni^{3+}$ ratio in layered Li(Ni,Mn,Co)$O_2$ cathodes for better electrochemistry. *J. Power Source* **2007**, *174*, 965–969. [CrossRef]
40. Ewald, P.P. The calculation of optical and electrostatic grid potential. *Ann Phys.* **1921**, *64*, 253–287. [CrossRef]
41. Verlet, L. Computer "Experiments" on Classical Fluids. I. Thermodynamical Properties of Lennard-Jones Molecules. *Phys. Rev.* **1967**, *159*, 98–103. [CrossRef]
42. Soo, S.P.; Idris, M.S.; Osman, R.A.; Rahmat, A. The Effect of Synthesis Temperature on Interlayer Mixing in Layered Rock Salt Cathode Materials $LiNi_{0.7}Mn_{0.1}Co_{0.2}O_2$ for Li-ion Batteries Application. *Mater. Sci. Forum.* **2015**, *819*, 155–160. [CrossRef]
43. Xiao, Y.; Liu, T.; Liu, J.; He, L.; Chen, J.; Zhang, J.; Luo, P.; Lu, H.; Wang, R.; Zhu, W.; et al. Insight into the origin of lithium/nickel ions exchange in layered $Li(Ni_xMn_yCo_z)O_2$ cathode materials. *Nano Energy* **2018**, *49*, 77–85. [CrossRef]
44. Pedone, A.; Malavasi, G.; Menziani, M.C.; Cormack, A.N.; Segre, U. A New Self-Consistent Empirical Interatomic Potential Model for Oxides, Silicates, and Silica-Based Glasses. *J. Phys. Chem. B* **2006**, *110*, 11780–11795. [CrossRef] [PubMed]
45. Huang, Y.; Liu, L.; Gao, M. Molecular dynamics study on the Li diffusion mechanism and delithiation process of $Li_2MnO_3$. *Solid State Ion.* **2020**, *346*, 115195. [CrossRef]
46. Gale, J.D. Gulp: A Computer Program for the Symmetry-Adapted Simulation of Solids. *J. Chem. Soc. Faraday Trans.* **1997**, *93*, 629–637. [CrossRef]
47. Asadi, A.; Aghamiri, S.F.; Talaie, M.R. Molecular dynamics simulation of a $Li_xMn_2O_4$ spinel cathode material in Li-ion batteries. *RSC Adv.* **2016**, *6*, 115354–115363. [CrossRef]
48. Fisher, C.A.J.; Prieto, V.M.H.; Islam, M.S. Lithium Battery Materials $LiMPO_4$(M = Mn, Fe, Co, and Ni): Insights into Defect Association, Transport Mechanisms, and Doping Behavior. *Chem. Mater.* **2008**, *20*, 5907–5915. [CrossRef]
49. Islam, M.S.; Driscoll, D.J.; Fisher, C.A.J.; Slater, P.R. Atomic-Scale Investigation of Defects, Dopants, and Lithium Transport in the $LiFePO_4$ Olivine-Type Battery Material. *Chem. Mater.* **2005**, *17*, 5085–5092. [CrossRef]
50. Armstrong, A.R.; Kuganathan, N.; Islam, M.S.; Bruce, P.G. Structure and Lithium Transport Pathways in $Li_2FeSiO_4$, Cathodes for Lithium Batteries. *J. Am. Chem. Soc.* **2011**, *133*, 13031–13035. [CrossRef]
51. Fisher, C.A.J.; Kuganathan, N.; Islam, M.S. Defect chemistry and lithium-ion migration in polymorphs of the cathode material $Li_2MnSiO_4$. *J. Mater. Chem. A* **2013**, *1*, 4207–4214. [CrossRef]
52. Tripathi, R.; Gardiner, G.R.; Islam, M.S.; Nazar, L.F. Alkali-ion Conduction Paths in $LiFeSO_4F$ and $NaFeSO_4F$ Tavorite-Type Cathode Materials. *Chem. Mater.* **2011**, *23*, 2278–2284. [CrossRef]
53. Perera, D.; Ganeshalingam, S.; Kuganathan, N.; Chroneos, A. A Computational Study of Defects, Li-Ion Migration and Dopants in $Li_2ZnSiO_4$ Polymorphs. *Crystals* **2019**, *9*, 563. [CrossRef]
54. Read, M.S.D.; Jackson, R.A. Derivation of enhanced potentials for uranium dioxide and the calculation of lattice and intrinsic defect properties. *J. Nucl. Mater.* **2010**, *406*, 293–303. [CrossRef]
55. Lee, E.; Lee, K.-R.; Lee, B.-J. An interatomic potential for the Li-Co-O ternary system. *Comput. Mater. Sci.* **2018**, *142*, 47–58. [CrossRef]
56. Van der Ven, A.; Ceder, G.; Asta, M.; Tepesch, P.D. First-principles theory of ionic diffusion with nondilute carriers. *Phys. Rev. B* **2001**, *64*, 184307. [CrossRef]
57. Ngala, J.K.; Chernova, N.A.; Ma, M.; Mamak, M.; Zavalij, P.Y.; Whittingham, M.S. The synthesis, characterization and electrochemical behavior of the layered $LiNi_{0.4}Mn_{0.4}Co_{0.2}O_2$ compound. *J. Mater. Chem.* **2004**, *14*, 214–220. [CrossRef]
58. Julien, C.; Mauger, A.; Zaghib, K.; Groult, H. Optimization of Layered Cathode Materials for Lithium-Ion Batteries. *Materials* **2016**, *9*, 595. [CrossRef] [PubMed]
59. Wang, D.; Xin, C.; Zhang, M.; Bai, J.; Zheng, J.; Kou, R.; Ko, J.Y.P.; Huq, A.; Zhong, G.; Sun, C.-J.; et al. Intrinsic Role of Cationic Substitution in Tuning Li/Ni Mixing in High-Ni Layered Oxides. *Chem. Mater.* **2019**, *31*, 2731–2740. [CrossRef]
60. Zhang, N.; Li, J.; Li, H.; Liu, A.; Huang, Q.; Ma, L.; Li, Y.; Dahn, J.R. Structural, Electrochemical, and Thermal Properties of Nickel-Rich $LiNi_xMn_yCo_zO_2$ Materials. *Chem. Mater.* **2018**, *30*, 8852–8860. [CrossRef]
61. Zheng, J.; Teng, G.; Xin, C.; Zhuo, Z.; Liu, J.; Li, Q.; Hu, Z.; Xu, M.; Yan, S.; Yang, W.; et al. Role of Superexchange Interaction on Tuning of Ni/Li Disordering in Layered $Li(Ni_xMn_yCo_z)O_2$. *J. Phys. Chem. Lett.* **2017**, *8*, 5537–5542. [CrossRef]
62. Lee, S.; Park, S.S. Atomistic Simulation Study of Mixed-Metal Oxide ($LiNi_{1/3}Mn_{1/3}Co_{1/3}O_2$) Cathode Material for Lithium Ion Battery. *J. Phys. Chem. C* **2012**, *116*, 6484–6489. [CrossRef]